2010 IEEE International Conference on Robotics and Automation
Anchorage Convention District
May 3-8, 2010, Anchorage, Alaska, USA

A Multi-Cell Piezoelectric Device for Tunable Resonance Actuation and Energy Harvesting

Thomas W. Secord, Anirban Mazumdar, and H. Harry Asada

Abstract— **Variable stiffness actuation and energy harvesting have been important yet separate challenges in robotics. Both functions are needed, however, for mobile robots on extended missions when actuators and generators must be used together. In this paper, we present a unique piezoelectric cellular system that combines motion generation and energy harvesting capabilities into a single, scalable device. Each of the discrete cellular units provides linear, contractile motion at 10% strain using the converse piezoelectric effect. These units may also be back-driven from environmental loading and thereby generate energy using the direct piezoelectric effect. Furthermore, each cell has the capability to toggle between a low stiffness ON state and a high stiffness OFF state, which allows an assembly of individual cells to tune both their static stiffness and structural resonant frequencies online. We demonstrate the effectiveness of our device for tuning both locomotion speed and the harvested power of an underwater flapping fin system.**

I. Introduction

One of the key challenges is bio-robotics is to develop a suitable linear, muscle-like actuator. This challenge arises because traditional electromechanical actuators cannot effectively recreate the muscle-like behaviors, such as inherent tunable stiffness, observed in biological systems. An additional drawback of traditional electromechanical actuators is that large gear ratios are often needed in order to match the force-speed characteristics of the actuator (i.e. motor) to that of the load. These large gear ratios lead to reduced efficiency of the motor to recover energy either from the environment or the robot's own kinetic and potential energy.

In this work, we present a modular device that is capable of overcoming the above difficulties in a unified package. Specifically, we present the design of a cellular, piezoelectric device that produces linear motion commensurate with natural muscle and also has the capability to effectively harvest energy from the environment. These two separate modalities of our device emerge from the piezoelectric ceramic material (PZT) and cellular architecture that we employ.

PZT is known for its desirable performance characteristics such as large stress capacity, long life cycle, capacitive impedance, and high bandwidth. The major drawback of PZT is that it has an inherently small active strain of approximately 0.1%. Natural muscle, on the other hand, has a much larger strain of 20%. To close the gap in strain performance between muscle and PZT, we have developed flexural strain amplification devices that enable PZT stacks to produce the desired level of strain at an acceptable tradeoff in bandwidth and stress. Rather than using one large piezoelectric stack, we have built an assembly of modular PZT units, called "cells," to produce large force and displacement.

Cellular architecture provides us with unique functionality and versatility that a single bulk actuator system cannot provide. For example, cellular architecture is beneficial for PZT stack actuators because the stacks cannot be scaled arbitrarily; only certain aspect ratios are manufacturable and robust to buckling or electrode failure. Another more general advantage of a cellular architecture is that our device can be scaled to meet the demands of many different robotic systems. For example, a robot requiring a large force actuator can be accommodated by using several cellular units in parallel. Finally, similar to muscle, a cellular architecture can simplify control by using local controllers that only need to switch a cell between an ON or OFF state [1], while the collective behavior of the parallel and serial cellular assembly is smooth and widely tunable.

In our design, we achieve widely tunable collective behavior by introducing a simple locking mechanism at each cell. Although PZT behaves in a linearly elastic fashion, the simple cell-level locking introduces a beneficial stiffness nonlinearity that leads to tunable static and dynamic behavior of the overall cellular system. Our cell level ON-OFF mechanism is a significant contrast to existing electrically-based approaches that achieve very precise, although limited range, stiffness tunability [2].

One of the salient features of our cellular PZT device is that it exhibits mechanical resonance. Mechanical resonance can be very useful for producing large amplitude periodic motions such as flapping [3], [4], running [5], [6], hopping [7], or swimming behavior [8] in bio-robotic systems. Our design not only exhibits the benefits of resonance but also allows the resonant frequency to be tuned over a wide range. As the resonant frequency is tuned, large amplitude motions can be produced across a spectrum of useful frequencies. From an energy harvesting standpoint, variable resonance allows the cellular device to tune its resonance to match the frequency of an imposed periodic forcing, which maximizes the energy harvested by the device.

T. W. Secord and A. Mazumdar are research assistants in the Dept. of Mechanical Engineering, at Massachusetts Institute of Technology, Cambridge, MA 02141 USA (617-253-3772; e-mail: secord@ mit.edu).

H. Harry Asada is a Professor of Mechanical Engineering at the Massachusetts Institute of Technology.

Our previous work in [9], [10], and [11] focused solely on actuation. This work extends our previous results in three main ways. First, we present a revised design of the variable stiffness mechanism. Second, we introduce the additional functionality of energy harvesting. Third, we apply the entire device to a variable resonance fin that can achieve both actuation and energy harvesting.

This paper is organized as follows. We begin with a description of the cellular, PZT device and explain both its actuation and energy harvesting modes of operation. We concurrently describe the lumped element dynamic models that are used to predict the system performance and aid in resonant frequency selection. In the final section of the paper, we present experimental results for tuning the resonance of an underwater fin used for both actuation and energy harvesting.

II. Variable Resonance Actuation

A. Basic Actuation Principle

Different sized individual cellular units are shown in Fig. 1(a) and an example of a muscle-like assembly of cells is shown in Fig. 1(b). The individual cells each produce more than 10% output length change (under fix-free end conditions), which is comparable to skeletal muscle. The largest of the cells is 85 mm across and produces nearly a 100 N maximum (i.e. blocking) force while the smallest cell is 30 mm across and produces a 5 N maximum force.

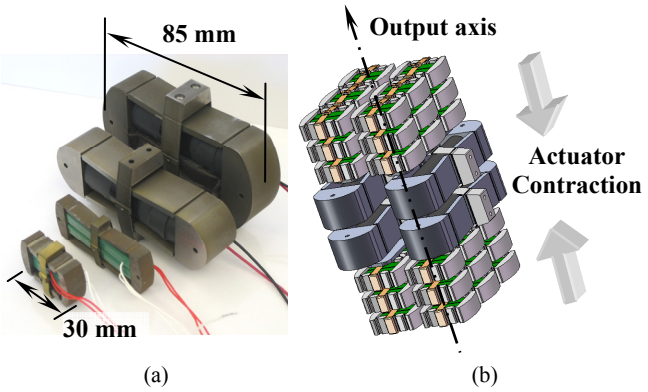

Fig. 1. (a) Different sized cellular units, each producing approximately 10% strain at different levels of force. (b) Muscle-like cellular assembly illustrating a mixed-cell connection topology.

The actuation operating principle for the cells is shown in Fig. 2 with the stacks removed for clarity. The cellular unit achieves large strain using two nested steel flexural amplifiers made using wire electrical discharge machining (EDM). The first flexural amplifier, shown in the left portion of Fig. 2, takes the small 0.1% expansion of the PZT stack along the *Y*-direction and converts it into and amplified motion along the *Z*-direction. This flexure is referred to as the first layer, non-inverting amplifier. The displacement amplification of this layer, denoted by g_1 is approximately $\cot(\theta_1)$ [11], where θ_1 is the angle of the flexural beam with respect to the *Y*-axis. In the *X*-*Z* plane, shown on the right side of Fig. 2, a second layer inverting amplifier flexure with a gain of $g_2 \approx \cot(\theta_2)$ is used to convert the amplified *Z*-axis motion from the first layer into a further amplified motion along the *X*-axis output. The overall displacement gain, G_f, is then given by $G_f = g_1 g_2$. The force at the output is attenuated by this same factor. Based on the analysis techniques described in [11], a reasonable tradeoff between force and displacement performance yields each of the gains to be approximately 10.

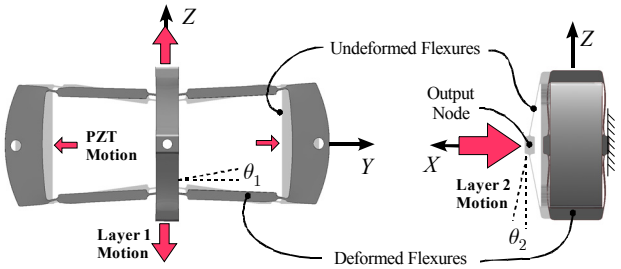

Fig. 2. Operating principle for the nested flexure amplification mechanism.

B. Variable Stiffness and Variable Resonance

Variable stiffness actuators have been developed by several groups (e.g. [6], [7], and [12]). However, a challenge in this development is to produce a large (i.e. >10) ratio of maximum stiffness to minimum stiffness. With a minor change to our basic PZT cell, we can attain a large stiffness tuning ratio (i.e. >100) and the multi-cell architecture allows us to easily adjust the device stiffness to various levels.

We impart variable stiffness characteristics to each cell by employing a stroke limiting beam as shown in Fig. 3(a). The stroke limiting beam introduces the compliance nonlinearity shown in Fig. 3(b). When the second layer flexures are not in contact with the stroke limiting beam, the cell is considered to be in its ON state and the equivalent compliance, *c*, of the flexures is $c = 1/k$, where *k* is the equivalent stiffness of the flexures as viewed from the output node. As voltage is applied to the PZT within the cell, the second layer flexure pulls in toward the stroke limiter. When the stroke limiter is reached at an inward contraction distance of x_{max} and additional voltage is applied, the compliance of the second layer flexures becomes very low (ideally zero) and the cell is then in its OFF state. The additional voltage is necessary to hold the flexure against the stroke limiter in the presence of tensile forces acting on the cell in the OFF state. Due to the capacitive nature of piezoelectric actuators, holding the device in the OFF state requires no current and therefore no power. Using this stroke limiting technique, each cell may readily toggle between a high compliance ON state and a low compliance OFF state.

In Fig. 3(b), notice that the main deviation of a real cell from the ideal case arises from the finite compliance of the stroke limiting beam. Nevertheless, the ratio of the highest stiffness to the lowest is very large due to the hard surface contact nonlinearity. When cells are arranged in series or in

parallel, the static stiffness of the assembly can be tuned from very rigid to very compliant in small increments.

Consider the simplest serial connection of $N = 2$ cellular units as shown schematically in Fig. 4(a) where both cells are shown in the ON state. Each cell in the strand is modeled by lumping the second layer flexure stiffness into a single element k while the mass of the PZT stacks and the flexures is lumped into a single mass m. The internal contraction force f_p is created as voltages are applied to the piezoelectric stacks. When a cell is turned OFF by contracting to the stroke limiter, its compliance becomes zero so it behaves only as translating mass.

There are $2^2 - 1 = 3$ possible activation configurations for the two cell system. The all OFF case is not considered and therefore the -1 is introduced. For simplicity, we will assume the cells are identical and we will denote the activation state of the strand with the vector $\boldsymbol{\alpha}$ where each element $\alpha_i \in \{0,1\}$ to represent OFF or ON in the usual binary sense. The number of ON units in a strand will be denoted by n.

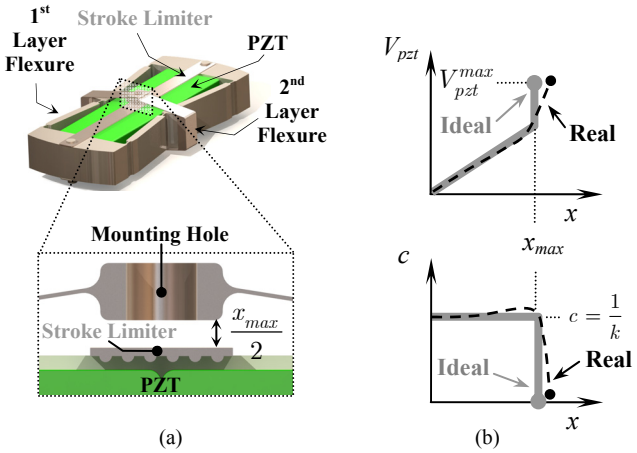

Fig. 3. (a) Design of a variable compliance cell using a stroke limiting beam. (b) Quasi-static voltage and compliance characteristics.

The static and dynamic models for each case are shown in Fig 4(b). The equivalent stiffness seen at the output of the serial strand is $k/2$ for the first case having $n = 2$ units ON and k for the second and third cases having $n = 1$ unit ON. Although only two discrete stiffness levels exist, the dynamic resonance behavior for each of the cases is quite different. Operating our system at a resonant frequency is highly beneficial because resonance produces large amplitude oscillatory motion that can be several times larger than the static stroke.

To find the resonant frequencies of serial systems we collect the node displacements x_i as shown in Fig. 4(a) into the vector $\mathbf{x}$ and use the homogenous equations of motion:

$$\mathbf{M}(\boldsymbol{\alpha})\ddot{\mathbf{x}} + \mathbf{K}\mathbf{x} = \mathbf{0}\,, \qquad (1)$$

where the squared resonant frequencies are given by the eigenvalues of the matrix product $\mathbf{M}^{-1}(\boldsymbol{\alpha})\mathbf{K}$. Note that the eigenvalues are modified based on activation dependent mass matrix $\mathbf{M}(\boldsymbol{\alpha})$.

The first case shown in Fig. 4(b) for our two-cell example represents a two degree of freedom vibratory system. If we normalize the resonant frequencies by $\sqrt{k/m}$, then the resonant frequencies for the first case are 1.62 and 0.62, while the second and third cases have resonant frequencies of 0.71 and 1.0 respectively. The set of achievable resonant frequencies becomes much more finely discretized as the number of cells in a strand, N, increases.

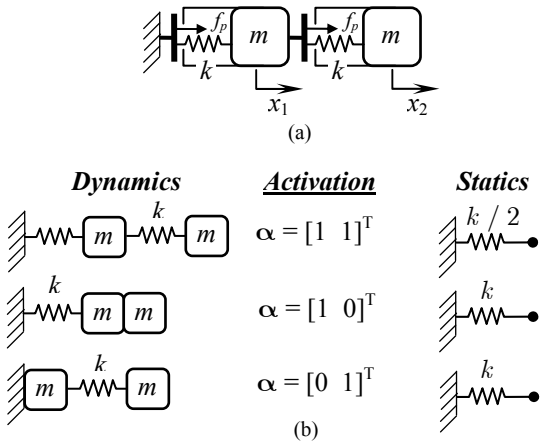

Fig. 4. (a) Serial strand connection of $N = 2$ cells (both shown ON). Note that k is the lumped second flexure stiffness and f_p is the force generated by the piezoelectric stacks through the amplification flexures. (b) Comparison of static and dynamic behavior for all possible, nontrivial activation configurations.

C. Selection of an ON-OFF Configuration for Actuation

For a strand of cells, we will denote the set of achievable resonant frequencies at a given static compliance level (i.e. a given number of ON units n) as $\Omega(n,N)$. The total set of all possible resonant frequencies $\Omega_T(N)$ is therefore

$$\Omega_T(N) = \bigcup_{n=1}^{N} \Omega(n,N)\,. \qquad (2)$$

For a robot to undergo periodic motion at a desired frequency, we first select the activation $\boldsymbol{\alpha}$ to correspond the element of $\Omega_T(N)$ closest to the desired frequency and then excite the ON cells at the desired frequency.

From a basic combinatoric analysis, the cardinality of $\Omega_T(N)$ grows as $N \cdot 2^{N-1}$ and this provides an unprecedented ability to tune resonant frequencies over a large, albeit discrete, range. In the next sub-section, we will illustrate how a similar resonance tuning idea can be utilized for energy harvesting.

III. Variable Resonance Energy Harvesting Principle

Piezoelectric devices have been studied extensively as a method for harvesting energy. Sodono, et al. [13] provide a concise overview of existing designs, where they point out that resonance is a key operating requirement for optimizing the power output of a harvesting device. Therefore,

harvesting energy across a band of frequencies requires tunable resonance. As a result, some variable resonance designs have been recently proposed. For example, Challa et al. [14] utilize a magnetically imposed stiffness to tune the resonant frequencies of a cantilever while a similar effect is achieved in [15] using a compressive axial preload on a vibrating piezoelectric bimorph. Purely electrical methods for achieving tunable resonance have also been explored [16]. Although existing designs are effective for their intended purpose, they operate only as harvesters, require an additional actuator and drive circuitry, and are tunable only within a narrow band of the structure's inherent fundamental resonant frequency. The approach that we describe in this section overcomes these difficulties using the piezoelectric cellular architecture.

A. Basic Energy Harvesting Principle

Several models exist to describe both the direct and converse piezoelectric effects [17]. A two-port model illustrating the PZT electromechanical transduction through an ideal flexure amplifier system (no flexure stiffness or inertia) is shown in Fig. 5. The figure shows that the electrical domain behavior for PZT is characterized by a capacitance C while the mechanical domain is characterized by an inherent mechanical stiffness k_{pzt}. The voltage-to-force coupling constant between the domains is denoted by β and the coupling between the second layer and the first layer is a lever with a displacement amplification ratio $G_f >> 1$.

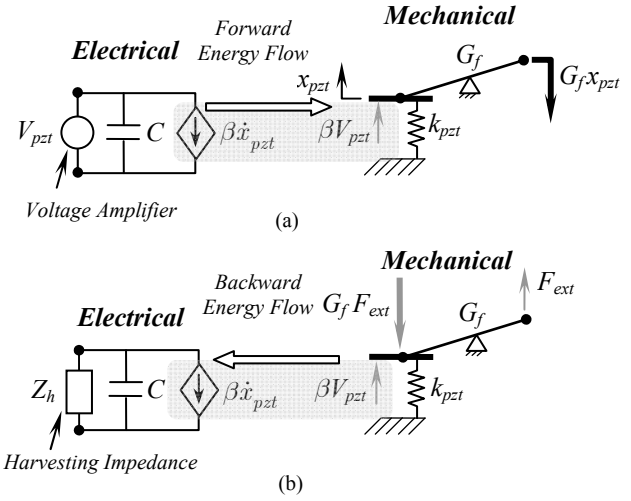

Fig. 5. (a) PZT converse effect where an applied voltage source is used to produce flexure displacements. (b) PZT direct effect where applied forces are used to generate a potential difference across an impedance. In both figures, the arrows indicate the primary direction of energy flow.

Fig. 5(a) shows the converse effect of PZT when we use our device as an actuator. For this case, we externally apply a PZT voltage V_{pzt} and use the large displacement gain, G_f, to amplify the PZT motion. For the harvesting case shown in Fig. 5(b), we again utilize the high gain to our advantage because forces applied at the second layer are transmitted back to the PZT stack through the same gain G_f. The generated PZT voltage is then applied across the harvesting impedance Z_h.

The principal advantages of our dual layer flexure energy harvesting approach are 1) compared to electromechanical actuators with large gear reducers, the frictional loss in the flexures is negligibly small and 2) the large amplification gain from the double-layer flexure cell, $G_f = g_1 g_2 > 100$, generates a high voltage, which is a critical requirement for effective energy harvesting. In [18], a single layer amplification stage is used with a gain of approximately 10. Our design significantly extends this gain while maintaining the advantages of a flexure-based system.

B. Variable Resonance Energy Harvesting

As a continuation of the example from II-B, a simple two-cell connection for variable resonance energy harvesting is shown in Fig. 6(a). The corresponding schematic model is shown in Fig. 6(b). For simplicity, we assume that energy is harvested across a purely resistive impedance $Z_h = R_h$. Using the PZT electromechanical transduction constant β, the electrical resistance may be reflected into the mechanical domain as the dashpot element b shown in Fig. 6(b). The resulting constant is $b = \beta^2 R_h$. As before, the mass m represents the combined flexure and PZT mass, while the stiffness k now accounts for the reflected PZT capacitance as well as the flexure stiffness.

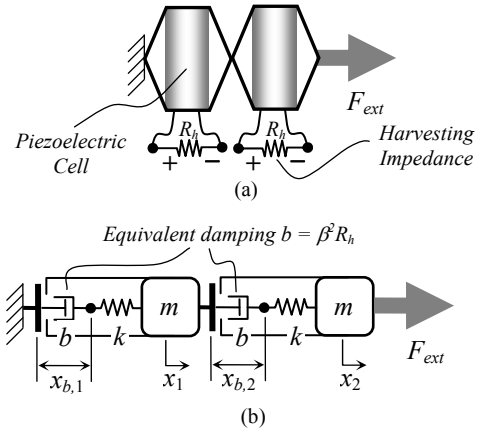

Fig. 6. (a) Two cells connected in series with harvesting resistances across the PZT electrodes. (b) Schematic model of the two cell harvesting system in (a).

The homogenous dynamic equations in (1) are now modified to include a damping matrix that also depends upon the activation of the strand.

$$\mathbf{M}(\boldsymbol{\alpha})\ddot{\mathbf{x}} + \mathbf{B}(\boldsymbol{\alpha})\dot{\mathbf{x}} + \mathbf{K}\mathbf{x} = \mathbf{0}\,. \tag{3}$$

Given full state knowledge of the system in (3), we may compute the internal damper displacements x_{bi}. Then, for a given serial configuration with n ON units, the instantaneous power harvested in the dashpot elements is given by summing the power from all ON units:

$$P = \sum_{i=1}^{n} b\dot{x}_{bi}^{\,2}\,. \tag{4}$$

Fig. 7 shows a plot of the harvested power computed from

(4) versus frequency and activation for the two cell example. The vertical power axis is scaled by the peak power over all possible configurations, $P_{max}(N)$, while the horizontal frequency axis is scaled by the single cell resonant frequency $\sqrt{k/m}$.

In Fig. 7, each ON-OFF activation of the cells provides different resonance characteristics. Recall from II-B that the undamped normalized resonant frequencies for a two-cell system are 0.62, 0.71, 1.0, and 1.62. Provided that the damping introduced by the harvesting resistance is not too large, the resonant peaks remain close to their undamped counterparts. The vertical bands in Fig. 7 that surround each peak indicate where the power drops to half of its maximum value for each resonance. If we take these four distinct ranges to be our effective harvesting frequency bands, then with only two cells we may expect to harvest energy over a 300% larger spectrum than would be possible with a single, fixed-resonance harvesting device.

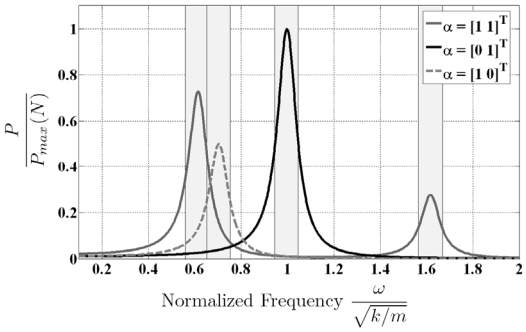

Fig. 7. Harvested power for various configurations of a two cell strand.

Fig. 7 also illustrates a more counter-intuitive aspect of the variable resonance harvesting mode of our device. Specifically, considering a single frequency sinusoid, it is possible to provide the most power to the resistance in the case where only the second cell is ON ($\boldsymbol{\alpha} = [0\ 1]^T$) and not the case with both cells ON ($\boldsymbol{\alpha} = [1\ 1]^T$), which indicates the importance of modeling for selecting a cellular activation $\boldsymbol{\alpha}$.

C. Selection of an ON-OFF Configuration for Harvesting

In general, the imposed forcing $F_{ext}(t)$ on a PZT-based harvester will not be a sinusoid of a single frequency, but rather it will have power distributed across a band of frequencies. In this instance, we denote the magnitude of the frequency spectrum of $F_{ext}(t)$ as $|F_{ext}(j\omega)|$ and we denote the transfer function from the applied force to relative velocity of the i^{th} dashpot (reflected electrical resistance) element as $H_i(s) = V_{rel,i}(s)/F_{ext}(s)$. These transfer functions will be dependent upon the activation $\boldsymbol{\alpha}$. Under these conditions, we take the optimal activation as

$$\boldsymbol{\alpha}^* = \arg\max_{\boldsymbol{\alpha}\in V_N} \left(\sum_{i=1}^{n} \int_0^{\infty} \left| H_i(\boldsymbol{\alpha}, j\omega) \right|^2 \left| F_{ext}(j\omega) \right| d\omega \right), \quad (5)$$

where the vector $\boldsymbol{\alpha}$ belongs to the set $V_{n,N}$, which is the set of binary vectors having N components, n of which are 1 and $(N - n)$ of which are 0. Note that $V_{n,N} \subset V_N$, which is the set of all binary vectors having N components. Eq. (5) assures that we maximize the total power harvested by the assembly considering all possible activations in V_N. As in Section II-C, this optimization search space is quite large and illustrates a major advantage of the cellular approach over existing designs with limited mechanical tunability.

IV. Underwater Robot Design Example

Underwater robotics provides an excellent domain for applying the cellular, muscle-like device discussed in the previous sections. In particular, the Office of Naval Research (ONR) recognizes that one of the major shortcomings in underwater bio-robotics is artificial muscle design [19]. Furthermore, deep sea autonomous vehicles can operate at depths exceeding 6000 meters, where pressures can exceed 65 MPa. At these depths, traditional thrusters encounter difficulties with seal leakage, corrosion, and overall breakdown. Piezoelectric materials can reduce these difficulties and lose only a fraction of their performance [20]. In the case of a biological swimming fish, there is also an approximate correlation of body natural frequencies with locomotion natural frequencies [21], [22], which makes variable resonance actuation especially appealing.

A. Experimental Apparatus

The experimental apparatus for an underwater flapping fin system is shown in Fig. 8 below. The figure shows the fin supported by a gantry arm that is free to rotate inside of a circular water tank. The fin itself is a NACA 0012 airfoil with a chord length of 150 mm and span of 76 mm. This fin is a reduced-scale version of the fin used in similar underwater experiments [23]. The fin is attached to a drive shaft, which extends out of the water to the actuator mounting frame on the end of the gantry arm shown in the inset of Fig. 8 and as a top view in Fig. 9. The actuators reside out of the water to alleviate the need for an underwater encapsulating structure.

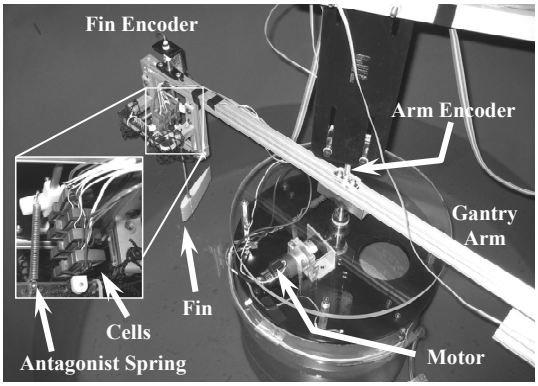

Fig. 8. Experimental apparatus for an underwater flapping fin system. The motor (shown attached) is decoupled from the center shaft for the actuation experiments. The tank diameter is 150 cm.

For energy harvesting experiments, the arm is driven by a single DC servomotor mounted to the center platform. For

actuation experiments, the motor is decoupled from the center shaft and the shaft is free to rotate such that the gantry arm is driven only by the torque produced from actuated fin thrust. The angle of the arm and the fin were measured using two separate magnetic encoders.

B. Actuation Experiments

1) Extension of the Dynamic Model

For experimental comparison, the simplified actuation model in Fig. 4 must be extended to include the effects of parasitic flexure damping and loading of the fin. The schematic model shown in Fig. 4 is modified by the addition of a dashpot element b_f in parallel with the stiffness k to represent flexure damping. The loading of the fin in the underwater environment is modeled as an equivalent mass m_L connected to ground through a parallel arrangement of a spring k_L and dashpot b_L. A top view of the actual fin system is shown in Fig. 9.

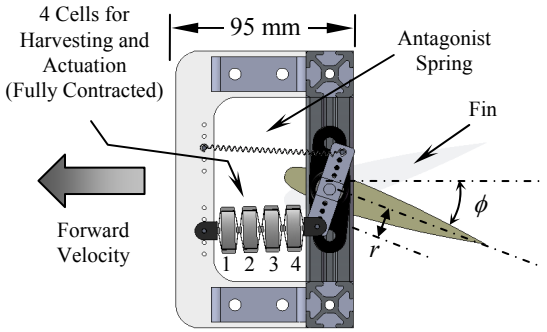

Fig. 9. Top view of fin system showing the major features of the design.

The rotational inertia of the fin, J_{fin}, was found using SolidWorks to be 2.62×10^{-4} kg·m^2. The added inertia from the water is estimated using

$$J_{added} \approx 0.036a\pi\rho h^2 L^3 , \qquad (6)$$

where ρ is fluid density of water, a is a dimensionless constant approximately equal to 1.25, h is the span of the fin, and L is the chord length of the fin [24]. Using a L = 150 mm and h = 76 mm in (6) yields $J_{added} = 2.8\times10^{-3}$ kg m^2.

The linearized angular drag coefficient b_{drag} (torque for a unit angular velocity) is given by modeling the fin as a flat plate oscillating at a frequency f with a drag coefficient of C_d and motion amplitude of ϕ_0:

$$b_{drag} = \frac{5\pi}{32}\rho C_d h L^4 f\phi_0 . \qquad (7)$$

Using C_d of 1.15 [25], f = 3 Hz, and ϕ_0 = 15°, we obtain b_{drag} = 1.71×10^{-2} N·m·s. The stiffness of the antagonistic spring, k_a, was measured directly to be 285.8 N/m and chosen to provide a 10 N tensile preload on the actuator cells when the system is at rest. The stiffness of the flexures, k, was measured to be 16.2×10^3 N/m while the flexure damping was estimated from a cell frequency response as b_f = 62 N·s/m. The rotational inertia and damping load effects were converted to the equivalent linear quantities by assuming small rotations of the fin and using the square of the moment arm of the actuators r where r = 12 mm (see Fig. 9).

2) Fin Flapping Amplitude versus Frequency

The first experiment measured fin amplitude as a function of frequency. We applied a sinusoidal chirp voltage input (0 to 150V from 0.2 Hz to 5 Hz) to all of the ON cells. For brevity and clarity of illustration, we tested only 2 of the possible 15 cases for activation: $[1\ 1\ 1\ 1]^T$ (all units ON) and $[0\ 0\ 1\ 1]^T$ (first two units grounded – cells 1 and 2 in Fig. 9). The activation of the cells was manually set using stroke limiting hard-stops similar to those shown in Fig. 3 only placed along the outside of the second layer flexure as in [10]. For these cells, the stiffness is profile is very high at zero voltage and very low at high voltages, which is the converse of the case discussed in II-B. The results of the experiment are shown in Fig. 10 below.

Fig. 10 shows that the fin system does indeed exhibit a resonance. For the case with all units ON ($\alpha = [1\ 1\ 1\ 1]^T$), the resonant peak resides at 2.26 Hz with a dynamic amplification ratio (peak to static displacement ratio) of 1.67. For the case with the first two units OFF ($\alpha = [0\ 0\ 1\ 1]^T$), the resonant frequency increased to 2.90 Hz, which is an upward tunability of 28%. For the second activation case, the dynamic amplification ratio is 1.78.

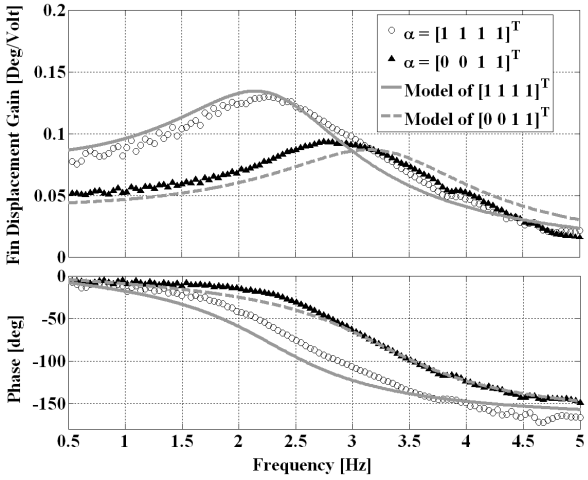

Fig. 10. Fin amplitude versus frequency for two cellular activations.

The predicted frequency response captures the dominant dynamic behavior of the system quite well. The slight disparity in predicted resonant frequencies and amplitudes is most likely due to uncertainty in the added mass and drag coefficients and the nonlinearity of the drag forces, which become particularly pronounced near resonance. Finally, note that we have assumed that the forward velocity of the fin does not appreciably affect the fin flapping amplitude.

3) Fin Forward Speed versus Frequency

The second experiment measured fin speed as a function of frequency for both the $[1\ 1\ 1\ 1]^T$ and the $[0\ 0\ 1\ 1]^T$ activations. In this experiment, we applied a fixed frequency sinusoidal voltage input (0V to 150V) to each of the ON cells and allowed the fin to reach a steady state velocity. The frequency was varied between 0.2 Hz to 5 Hz using 20

linearly spaced points. The results are shown in Fig. 11.

Fig. 11 shows that the various activations provide different peak velocities, but both velocities are the result of large amplitude resonant oscillations of the structure. For the $[1\ 1\ 1\ 1]^T$ case, the maximum forward velocity was 0.11 m/s, while for the $[0\ 0\ 1\ 1]^T$ case, the maximum forward velocity was 0.089 m/s. The slight increase in velocity near 3.3 Hz for the $[1\ 1\ 1\ 1]^T$ case and near 3.9 Hz for the $[0\ 0\ 1\ 1]^T$ case is most likely due to an additional unmodeled structural resonance that shifts with activation yet is unobservable from the fin encoder readings.

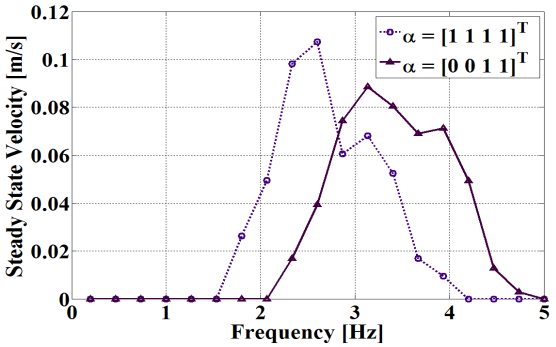

Fig. 11. Fin steady state velocity versus frequency for two cellular activations.

The velocities of our fin system (0.71 fin lengths per second) compare favorably with existing high performance designs (e.g. [26] – 0.37 body lengths per second) and illustrate that speed may be tuned by adjusting resonant frequencies. Moreover, the frequency response magnitude curves in Fig. 10 intersect near 3 Hz while the velocity curves in Fig. 11 also intersect near 3 Hz (2.8 Hz) with a steady state velocity of 0.069 m/s. If this were the desired velocity, then the activation $[0\ 0\ 1\ 1]^T$ is preferable because it utilizes fewer ON units and therefore less power at the given frequency. However, if maximum speed is desired, an activation of $[1\ 1\ 1\ 1]^T$ would be more appropriate.

C. Energy Harvesting

There are many sources of energy in aquatic environments, some of which include ocean currents, wavy stream currents, and unsteady flow around objects. Our system may be used to harvest energy from any such flows. To illustrate this functionality, the test apparatus shown in Fig. 11 was also used to perform energy harvesting experiments with the fin system. For these experiments, we coupled the drive motor to the center shaft of the gantry arm and applied sinusoidal voltages to the motor (0 to 24V) at frequencies ranging from 0.2 Hz to 3 Hz. The gantry arm drove the fin forward resulting in fin deflection due to drag forces caused by the relative velocity of the fin and the water. The fin deflection results in reaction forces borne by the actuators and voltages generated at the PZT stacks.

A 23.4 k Ω resistor was placed across each of the cells and the output power across the resistance at cell 4 (see Fig. 9) was acquired using a cRIO system (National Instruments). The resistance value was based on modulus matching the piezoelectric electrical capacitive impedance using

$$R_h = \frac{1}{2\pi f_{ave} C}, \tag{8}$$

where f_{ave} is the average frequency for the experiment (taken as 3 Hz), and C is the electrical capacitance of the stack (measured using an impedance analyzer to be 9 μF). Such modulus matching is consistent with much of the piezoelectric energy harvesting literature (e.g. [14], [15], [16]), but is known to be sub-optimal because it does not account for reactive power effects [27].

The results of a representative harvesting experiment are shown in Fig. 12 below. The top portion of the figure shows a time profile of the velocity imposed upon the fin using the motor-driven gantry arm. The two experiments yielded nearly identical velocity profiles. The power spectra of the fin velocity data reveal that the dominant frequency components reside at 1.25 Hz and 8.75 Hz.

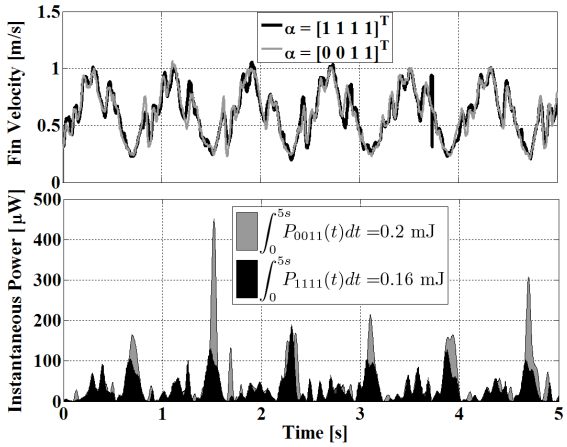

Fig. 12. Plot of the imposed fin velocity and instantaneous power across the fourth cell's harvesting resistor for two representative 5 s experiments, one having $[1\ 1\ 1\ 1]^T$ and the other having $[0\ 0\ 1\ 1]^T$.

The lower portion of Fig. 12 shows the resulting instantaneous power at the harvesting resistance as well as its integral (total energy) for the experiment. In the case with all units ON, the instantaneous power was appreciably lower than the case with the first two units grounded because the all-ON case is not excited as effectively by the higher frequency component of the imposed velocity. Hence, as in the example of III-B, turning OFF units leads to a higher resonance that is more effective for the given forcing condition. For this particular example, the total energy for $[0\ 0\ 1\ 1]^T$ (0.2 mJ) is 25% greater than that of the all ON case $[1\ 1\ 1\ 1]^T$ (0.16 mJ) over the 5 s duration. However, if we assume that all cells harvest an identical amount of energy, then the all ON case is still preferable because the all ON case would yield 0.64 mJ whereas the two OFF case would only yield 0.40 mJ. This example highlights the importance of the activation selection criteria given in (5).

D. Discussion

The experimental results presented in this section illustrate

several key points of our design:

- Resonance of an underwater fin system can be achieved and widely tuned with our cellular design.
- Resonance is highly beneficial in underwater flapping because it greatly increases forward velocity and effectively harnesses stored kinetic and potential energy in the system.
- Tuning forward velocity of an underwater flapping system requires only simple ON-OFF configuration changes. Furthermore, high swimming velocity may be maintained by turning units OFF and utilizing the shifted resonance.
- Energy harvesting can be achieved using the same cellular system as used for motion generation of a fin.
- Tuning the cell activation states can significantly increase the harvested power by changing the frequency response characteristics of the fin system.

V. Conclusions and Future Work

This paper highlights the significant benefits of tuning stiffness and resonance of a PZT-based cellular system for bio-robotics applications involving periodic motion. The features of our device are clearly illustrated using an underwater flapping fin system that achieves tunable resonance forward velocity swimming as well as tunable energy harvesting characteristics.

In the future, we intend to explore flexible fin systems and vortex based energy harvesting using the hydrodynamic effects described in [23]. Further improvements to our harvesting design involve real-time impedance matching algorithms, battery charging capability, and fin configuration changes to enhance the forces transmitted from a flow to the fin. Improvements to our actuation system involve larger arrays of cells leading to larger motion amplitude and more tunability. The overarching goal of our work is to develop a fully assembled, flexible fin, swimming robot. Overall, this paper illustrates that our combined cellular actuator and energy-harvesting device performs two ubiquitous functions in a single package.

Acknowledgment

The second author would like to acknowledge the NSF Graduate Research Fellowship Program.

References

[1] K.-J. Cho, J. Rosemarin, and H. H. Asada, "Design of vast DOF artificial muscle actuators with a cellular array structure and its application to a five-fingered robotic hand," *Proceedings - IEEE International Conference on Robotics and Automation*, pp. 2214 - 2219, 2006.

[2] D. Guyomar, M. Lallart, and T. Monnier, "Stiffness tuning using a low-cost semiactive nonlinear technique," *IEEE/ASME Transactions on Mechatronics*, vol. 13, no. 5 Part 0, pp. 604-607, 2008.

[3] J. Yan, R. Wood, S. Avadhanula, M. Sitti, R. Fearing, "Towards flapping wing control for a micromechanical flying insect," *Proceedings – International Conference on Robotics and Automation*, vol. 4, pp. 3901-3908, 2001.

[4] K. K. Issac and S. K. Agrawal, "An investigation into the use of springs and wing motions to minimize the power expended by a pigeon-sized mechanical bird for steady flight," *Journal of Mechanical Design*, vol. 129, no. 4, pp. 381-389, 2007.

[5] M. H. Raibert, *Legged robots that balance*. MIT Press, Cambridge, MA, 1986.

[6] J. Hurst, J. Chestnutt, and A. Rizzi, "An actuator with physically variable stiffness for highly dynamic legged locomotion," *Proceedings - IEEE International Conference on Robotics and Automation*, vol. 5, pp. 4662-4667, 2004.

[7] R. Van Ham, B. Vanderborght, M. Van Damme, B. Verrelst, and D. Lefeber, "MACCEPA, the mechanically adjustable compliance and controllable equilibrium position actuator: Design and implementation in a biped robot," *Robotics and Autonomous Systems*, vol. 55, no. 10, pp. 761-768, 2007.

[8] P. Valdivia y Alvarado and K. Youcef-Toumi, "Design of machines with compliant bodies for biomimetic locomotion in liquid environments," *Journal of Dynamic Systems, Measurement and Control*, vol. 128, no. 1, pp. 3-13, 2006.

[9] T. W. Secord and H. H. Asada, "A variable stiffness PZT cellular actuator with tunable resonance for cyclic motion tasks," *Proceedings - IEEE International Conference on Robotics and Automation*, pp. 176-181, 2009.

[10] T. W. Secord and H. H. Asada, "Cellular muscle actuators with variable resonant frequencies," *To appear in Proceedings – Robotics: Science and Systems*, 2009.

[11] T. W. Secord, J. Ueda, and H. H. Asada, "Static analysis of an artificial muscle system based on pzt strain amplification," *Proceedings of SPIE - The International Society for Optical Engineering*, vol. 6932, 2008.

[12] J. Choi, S. Park, W. Lee, and S.-C. Kang, "Design of a robot joint with variable stiffness," *Proceedings – IEEE International Conference on Robotics and Automation*, pp. 1760-1765, 2008.

[13] H. Sodano, D. Inman, and G. Park, "A review of power harvesting from vibration using piezoelectric materials," *Shock and Vibration Digest*, vol. 36, no. 3, pp. 197-206, 2004.

[14] V. Challa, M. Prasad, Y. Shi, and F. Fisher, "A vibration energy harvesting device with bidirectional resonance frequency tunability," *Smart Materials and Structures*, vol. 17, no. 1, p. 15035, 2008.

[15] E. Leland and P. Wright, "Resonance tuning of piezoelectric vibration energy scavenging generators using compressive axial preload," *Smart Materials and Structures*, vol. 15, no. 5, p. 1413, 2006.

[16] W. Wu, Y. Chen, B. Lee, J. He, and Y. Peng, "Tunable resonant frequency power harvesting devices," in *Proceedings of SPIE*, vol. 6169, p. 61690A, 2006.

[17] B. Richter, J. Twiefel, and J. Wallaschek, "Piezoelectric equivalent circuit models," in *Energy Harvesting Technologies* (S. Priya and D. Inman, eds.), ch. 4, pp. 107-128, Springer, 2008.

[18] J. Feenstra, J. Granstrom, and H. Sodano, "Energy harvesting through a backpack employing a mechanically amplified piezoelectric stack," *Mechanical Systems and Signal Processing*, 2007.

[19] P. Bandyopadhyay, "Trends in biorobotic autonomous undersea vehicles," *IEEE Journal of Oceanic Engineering*, vol. 30, no. 1, pp. 109-139, 2005.

[20] S. Balakrishnan and C. Niezrecki, "Investigation of Thunder Actuators as Underwater Propulsors," *Journal of Intelligent Material Systems and Structures*, vol. 13, no. 4, p. 193, 2002.

[21] B. Ahlborn, *Zoological physics*. Chapter 6, Springer, 2004.

[22] J. Long and K. Nipper, "The Importance of Body Stiffness in Undulatory Propulsion," *Integrative and Comparative Biology*, vol. 36, no. 6, pp. 678-694, 1996.

[23] D. Beal, F. Hover, M. Triantafyllou, J. Liao, and G. Lauder, "Passive propulsion in vortex wakes," *Journal of Fluid Mechanics*, vol. 549, pp. 385-402, 2006.

[24] A. Korotkin, *Added Masses of Ship Structures*. Springer, 2008.

[25] J. Newman, *Marine Hydrodynamics*. The MIT press, 1977.

[26] A. Mazumdar, P. Alvarado, and K. Youcef-Toumi, "Maneuverability of a robotic tuna with compliant body," *Proceedings - IEEE International Conference on Robotics and Automation*, pp. 683-688, 2008.

[27] J. Brufau-Penella and M. Puig-Vidal, "Piezoelectric Energy Harvesting Improvement with Complex Conjugate Impedance Matching," *Journal of Intelligent Material Systems and Structures*, vol. 20, no. 5, p. 597, 2009.